

Strain can significantly regulate the electronic, valley, and magnetic properties of materials [33–42]. Among them, straintronics leverages mechanical strain to manipulate the electronic properties of materials, which are adopted to develop energy-efficient, multifunctional electronic devices and flexible electronics [33–39]. Once straintronics is introduced at atomic level for van de Waals (vdW) heterostructures, it provides an effective and universal approach to modulate the electronic properties, including in-plane strain, out-of-plane strain and heterostrain [39]. Considering the great impact of atomic geometries on the physical properties of Bi(110), it is expected that the strain induced by the interlayer interaction in the epitaxial film will benefit the precise control of its electronic properties.

In this work, we have constructed an epitaxial vdW heterostructure composed of 2–3 BL Bi(110) and ferromagnet Fe₃GeTe₂ by molecular-beam epitaxy (MBE) method. It is demonstrated that heterostrain is generated between Bi(110) in BP structure and Fe₃GeTe₂ with in-plane hexagonal symmetry due to their lattice mismatch. Scanning tunneling microscopy (STM) studies show that both periodic biaxial strain and vibration of the buckling height h are generated. The strain-driven control of the electronic properties is also observed via STM and scanning tunneling spectroscopy (STS) method. Combined with density functional theory (DFT) calculations, it turns out that strain can effectively modulate the band gap of Bi(110) periodically, providing an effective method for adjusting the atomic geometries and electronic properties of 2–3 BL Bi(110). In addition, we have also investigated the magnetic proximity effect of the magnetic substrate Fe₃GeTe₂ on the Bi(110) thin film. This work of constructing heterostrain structure provides a pathway for modifying the electronic properties of Bi(110) at atomic scale, which could promote its applications of straintronic or nanoelectronics devices with potential novel functionalities.

2 Experimental section

2.1 Synthesis of Fe₃GeTe₂ single crystal

High-quality Fe₃GeTe₂ single crystals were synthesized via chemical vapor transport method [43, 44]. High-purity Fe (99.99%), Ge (99.99%), and Te (99.99%), in a stoichiometric ratio of 3:1:2 with iodine as the transport agent were sealed in an evacuated quartz tube. The tube was placed into a two-zone horizontal furnace with the hot end at 770 °C and the cold end at 680 °C. The obtained crystals were on the millimeter scaled (2–3 mm) and quasi-hexagonal plates.

2.2 Bi(110) thin film growth

A Fe₃GeTe₂ single crystal flake was *in-situ* cleaved

under ultra-high vacuum (UHV) ($< 5.0 \times 10^{-10}$ Torr). And then, high-purity Bi (99.99%) was deposited onto the surface of Fe₃GeTe₂ at room temperature using a standard Knudsen cell. The temperature of Knudsen cell is approximately 500 °C during the growth of about 120 min.

2.3 STM/STS measurements

STM and STS measurements were performed using a low-temperature STM system under UHV at 77 K. The STM tip was prepared using chemically etched W-wires and cleaned in vacuum. All the STM images were obtained in constant current mode. The STS differential conductance (dI/dV) and STS maps were obtained using the constant-height mode with the feedback loop closed with lock-in detection by applying modulation to the tunneling at 973 Hz. All data was obtained at 77 K. All the STM images were analyzed by WSxM software [45].

2.4 DFT calculations

The first-principles calculations were performed by using the Vienna *ab initio* simulation package (VASP) with the projector augmented wave approach (PAW) and the Perdew–Burke–Ernzerh (PBE) generalized-gradient approximation (GGA) [46–48]. The cutoff energy of the plane-wave expansion of the basic functions was set to 350 eV. $7 \times 7 \times 1$ Γ -centered Monkhorst–Pack k -point meshes were used to sample the BZ of Bi(110) unit cells. Based on experimental lattice parameters, all the atom position were fully relaxed with DFT-D3 vdW correction [49] until the residual force of each atom is smaller than 0.01 eV/Å. The spin orbital coupling effect is considered in our electronic structure calculations. The size of the vacuum layer is 15 Å.

2.5 Strain analysis

Strain distribution in the Bi(110) thin films was analyzed using Strain++ software [50].

3 Results and discussion

We firstly demonstrate the lattice structure of the Bi(110)/Fe₃GeTe₂ heterostructure. As shown in the crystal structure of Fe₃GeTe₂ [Fig. 1(a)], Te atoms from the top layer arrange in hexagonal structure, with a lattice constant of about 4.0 Å. Following exfoliation under UHV conditions, Fe₃GeTe₂ surface was characterized using STM, and showing a hexagonal lattice with lattice constant of 4.0 Å [Figs. 1(b, c)]. Subsequently, 2–3 BL Bi(110) film was fabricated by MBE method on the *in-situ* cleaved Fe₃GeTe₂. Bi(110) exhibits a black phosphorus (BP)-like structure [Fig. 1(d)], characterized by an

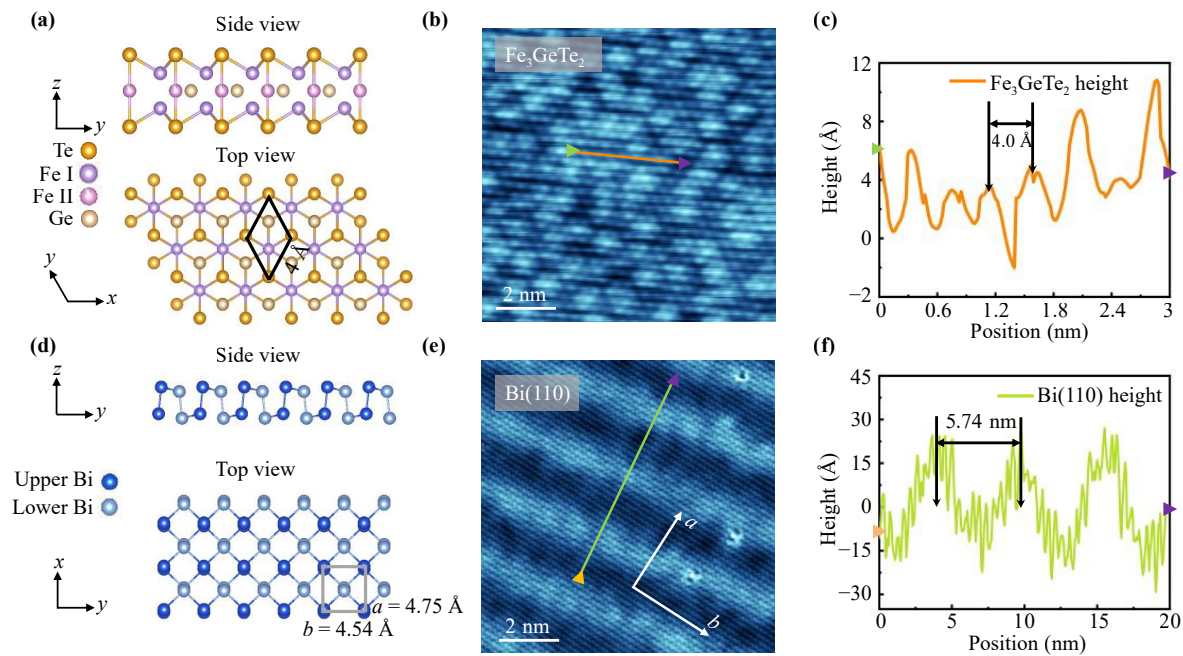


Fig. 1 (a) Schematic diagrams of the crystal structure of Fe_3GeTe_2 and the upper and down panel are the side view and top view, respectively. (b) The atomic-resolution STM topography of Fe_3GeTe_2 substrate. (c) The line profile obtained from the Fe_3GeTe_2 surface taken along orange line in Fig. 1(b). (d) Schematic diagrams of the lattice structure of Bi(110) and the up and down diagrams are the side view and top view, respectively. (e) The atomic-resolution STM topography of Bi(110). (f) The line profile taken along the green line in (e) from Bi(110) strain stripe area.

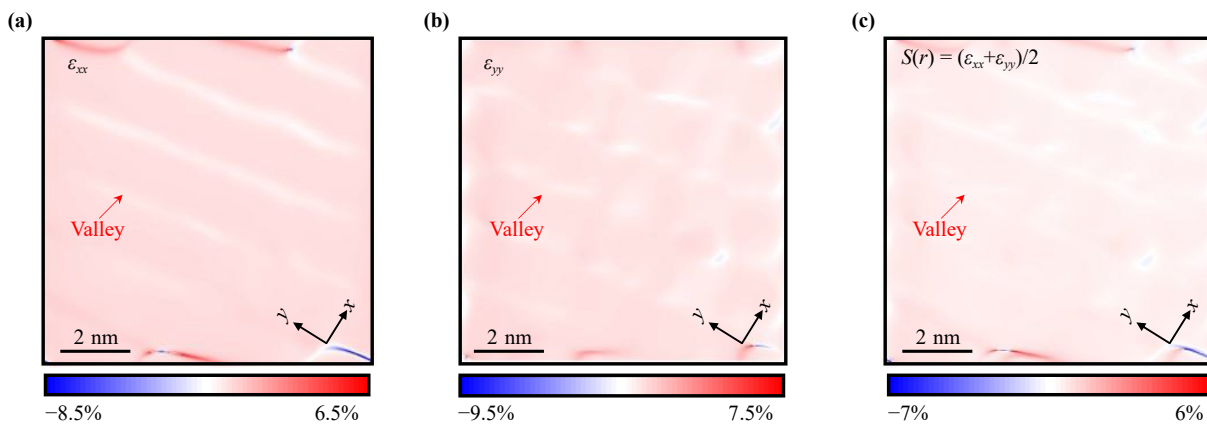


Fig. 2 The strain distribution for the Bi(110) film shown in Fig. 1(d). (a) Strain distribution in the x -axis. (b) Strain distribution in the y -axis. (c) Sum of strain distributions in the Bi(110) film.

orthorhombic lattice with lattice parameters $a = 4.75 \text{ \AA}$ and $b = 4.54 \text{ \AA}$. Both terminated sides of a BL Bi(110) layer contains two Bi atoms: one is positioned at the corner of the rectangular cell and the other is positioned close to the center with its deviation depending on the degree of buckling height h . Notably, the changes of this atomic geometry have significantly influenced its electronic and topological properties in previous studies [20, 25–27]. As shown in Fig. 1(e), the most apparent feature of the STM image of Bi(110) film is the stripe structure (named as Stripe I), which exhibits a characteristic peri-

odicity of 5.74 nm [Fig. 1(f)].

Periodic strain is expected to exist together with stripe I. Strain distribution is then analyzed by Strain++ software based on Geometric Phase Analysis (GPA) algorithm [50] (more details in Supplemental note 1). The lattice directions a and b are selected as the x and y axes, respectively. The typical area of Bi(110) shown in Fig. 1(e) is analyzed in Fig. 2. As shown in Figs. 2(a) and (b), tensile strain around 5% exists along the x -axis direction (ϵ_{xx}) and 4% exists along the y -axis direction (ϵ_{yy}), mainly on the stripe I. Near-zero strains

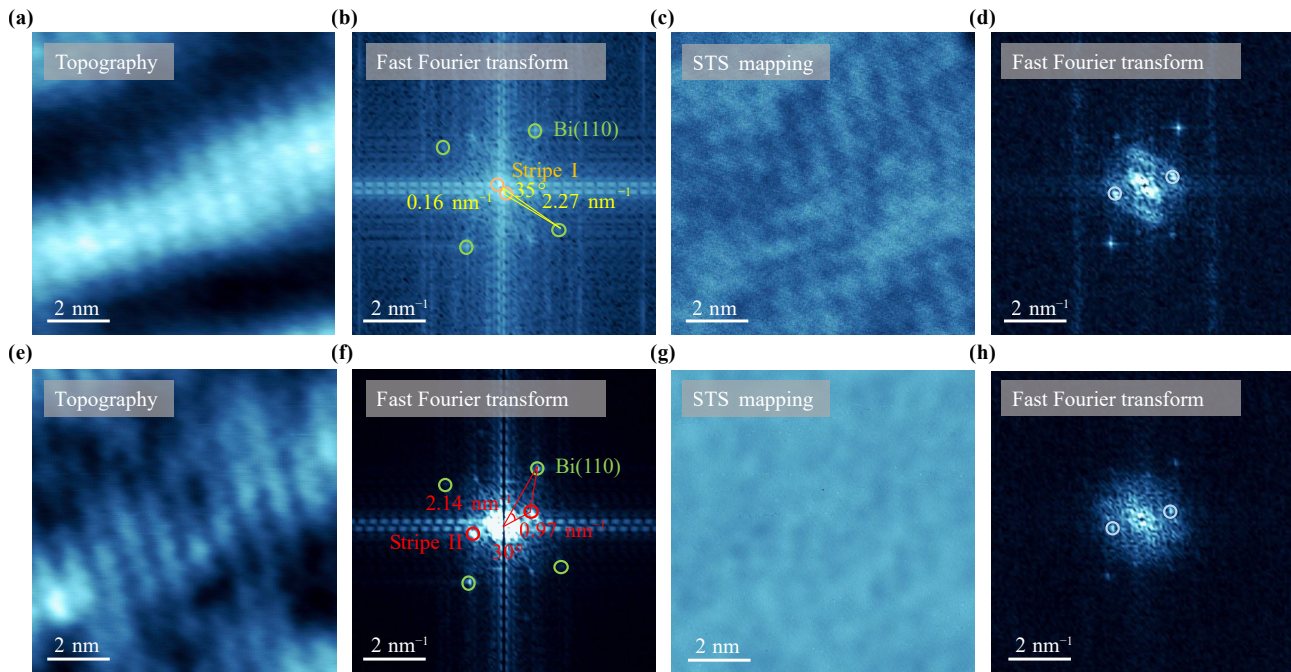


Fig. 3 (a) The atomic-resolution STM topographic image of Bi(001) surface with strain stripe, when the sample bias = 600 mV, tunnelling current $I = 500$ pA. (b) The fast Fourier transform (FFT) result of (a). (c) The STS mapping at 600 mV, tunnelling current $I = 500$ pA. (d) The FFT result of (c). The blue labels are represented to Stripe II. (e) The STM topography of strain stripe, when the sample bias = -100 mV, tunnelling current $I = 500$ pA. (f) FFT result of (e). (g) The STS mapping at -100 mV, tunnelling current $I = 500$ pA. (h) FFT result of (g). The blue labels are represented to Stripe II.

are observed at the valley regions. It is notable that periodic tensile strain features along the y -axis direction are observed on the whole area, rather than ε_{xx} mainly limited on stripe I. The surface stress across the entire characterized region was calculated by $S(r) = (\varepsilon_{xx} + \varepsilon_{yy})/2$. Therefore, the strain distribution of the Bi(110) film is determined to be bidirectional, which can be observed more clearly in the $S(r)$ strain analysis as illustrated in Fig. 2(c). A comparison between the strain distribution analysis results in Fig. 1(e) and Fig. 2 reveals that the strain in the stripe and valley regions are tensile and nearly zero, respectively.

The strain-induced electronic state modulation in Bi(110) thin films was then investigated using STM and STS methods. A series of topographic images and conductance maps taken at the same region under various biases are presented in Figure S2. The stripe feature was found exhibiting strong bias-dependent in both the surface topography and the electronic state distribution. As shown in Fig. 3(a), when scanned at sample bias 600 mV, stripe I is dominant on the surface topography. The corresponding Fast Fourier transform (FFT) analysis [Fig. 3(b)] reveals that stripe I exhibit a 35° angular relationship with respect to b axis. While stripe I is indistinct at 100 mV sample bias as shown in Fig. 3(d). As the apparent height profile represents a superposition of surface topography and electronic states, the variation

of the apparent height indicate the electronic states of Bi(110) have been effectively modulated by stripe I. Meanwhile, an additional stripe structure (named as stripe II) can be found both in Figs. 3(a) and (d). This additional stripe II shows around 30° angle with respect to a -axis, as revealed by the FFT image in Fig. 3(e). Stripe II can also be observed in the conductance maps [Figs. 3(c) and (f)] and in their corresponding FFT images [Figs. 3(d) and (g)]. More surface topography and electronic state distribution results imply that stripe II can be observed at most of the sample bias, except those that are close to zero bias [Figs. S2(e, i, m)]. Considering Bi(110) normally exhibit semiconducting properties, it is reasonable to believe that stripe II feature is not bias-dependent, indicating stripe II may be related to strain distribution. This interpretation agrees with the strain analysis where the periodic tensile strain along y axis in ε_{yy} and $S(r)$ is confirmed. Above results demonstrate that the bidirectional periodic strain of Bi(110) has periodically modulated its electronic structures.

The size of bandgap is one of the most important electronic parameters of Bi(110) controlling its physical properties, that can be modulated by strain and interlayer coupling. Thus, the electronic structure of Bi(110) under various strain situations (stripe and valley region shown in Fig. S3) was investigated by STS method. The bandgap

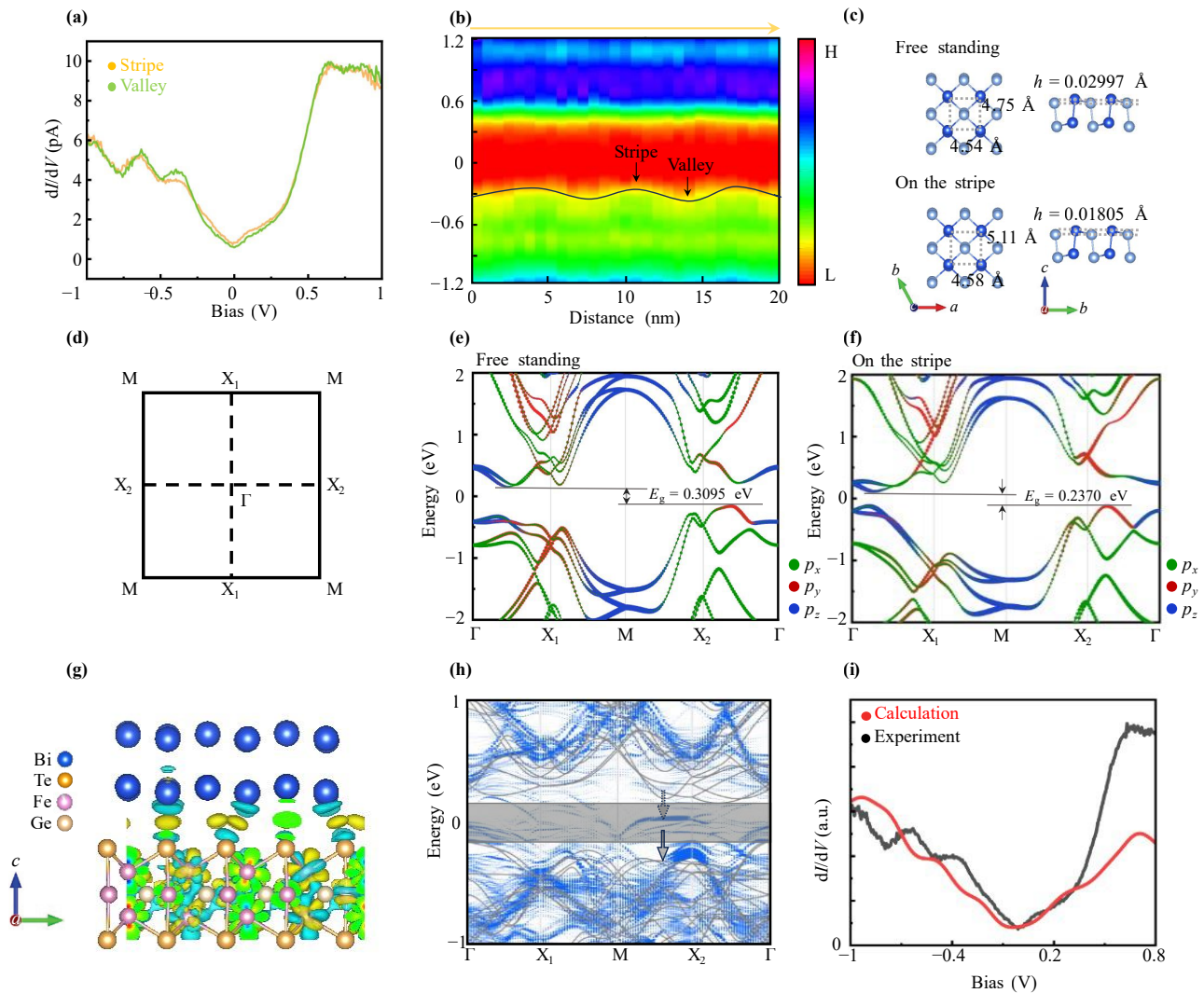


Fig. 4 (a) The typical dI/dV spectra taken at the positions indicated by the color dots in Fig. S3(a). (b) 2D plot of tunnelling spectra measured along the orange arrow line in (a). (c) Schematic diagram of the free standing Bi(110) (upper) and stripe Bi(110) (down) lattice structure, showing the lattice structure constant and atomic buckling height respectively. (d) Schematic diagram of the Brillouin zone for Bi(110). (e) DFT orbital-resolved band structure of free standing Bi(110). (f) DFT orbital-resolved band structure of Bi(110) lattice on the stripe. (g) The differential charge distribution results of Bi(110)/Fe₃GeTe₂ heterostructure. The blue isosurfaces indicate regions of electron depletion, whereas the yellow isosurfaces correspond to regions of electron accumulation. (h) DFT-calculated band structures of the Bi(110)/Fe₃GeTe₂ heterostructure. The gray bands represent the band structure of DFT-relaxed Bi(110) without considering the Fe₃GeTe₂ substrate, and the blue bands represent the projected electronic states of Bi(110) with the Fe₃GeTe₂ substrate. (i) Experimental and computational dI/dV spectra.

measured on stripe I and its valley of Bi(110) is remarkably different, as shown in Fig. 4(a). The strain-induced bandgap modulation in Bi(110) film can be further confirmed by the line conductance map taken across one stripe I [Fig. 4(b)]. The bending and shifts of the valence band maximum (VBM) confirm that the bandgap is smaller on the stripe than that at the valley, indicating that the band gap modulation is related to the strain cross stripe I.

To further understand the strain-induced modulation of the band gap, DFT calculations were performed on

both free-standing Bi(110) ($a = 4.75 \text{ \AA}$, $b = 4.54 \text{ \AA}$, $h = 0.02997 \text{ \AA}$) and Bi(110) under strain conditions derived from the lattice constants observed in the stripes ($a = 5.11 \text{ \AA}$, $b = 4.58 \text{ \AA}$, $h = 0.01805 \text{ \AA}$) [Fig. 4(c)], which is consistent with Strain++ analysis in Fig. 2. DFT orbital-resolved band structure can reveal distinct orbital contributions to the conduction and valence bands with different buckling height h . The Bi(110) Brillouin zone is showed in Fig. 4(d). Specifically, the CBM is dominated by Bi p_x and p_z orbital contributions, while the VBM exhibits prominent p_y orbital character [Figs. 4(e, f)].

Therefore, the strain-induced lattice distortion is expected to modify the hybridization of p_x and p_y orbitals, bond lengths between bismuth atoms and buckling height h . According to the calculated results, the tensile strain along the y -axis ($b = 4.58 \text{ \AA}$) influences p_y orbitals at the VBM for Bi(110) under strain, while tensile strain along the x -axis ($a = 5.11 \text{ \AA}$) suppress contribution of p_x orbital at the CBM. In addition, the decrease of buckling height h enhances the contribution of p_z orbital at the VBM. This asymmetric orbital response leads to a calculated bandgap decrease of 0.07 eV compared to free-standing Bi(110), which is consistent with the experimentally observed trend of band gap enlargement in tensile strain along a lattice direction and b lattice direction (on the stripes). Combining experimental characterizations and DFT calculations, the periodic strain not only modifies the atomic configurations including in-plane lattice constant as well as buckling height h of Bi(110), but periodically tunes its electronic properties.

Furthermore, the influence of the magnetic substrate Fe_3GeTe_2 on Bi(110) was investigated through DFT calculations. Figure 4(g) shows the calculated differential charge distribution of BL Bi(110) on Fe_3GeTe_2 , in which apparent charge transfer can be observed at the Bi/ Fe_3GeTe_2 interface. And the charge distribution of the Fe I atoms on the upper and lower surfaces of Fe_3GeTe_2 differ due to the existence of BL Bi(110), indicating unignorable interaction between the FeI atom layer (upper layer near the Bi(110)) and Bi(110). Additionally, the band structures of Bi(110) with same lattice condition without [represented by grey lines in Fig. 4(h)] and with [represented by blue dots in Fig. 4(h)] considering the Fe_3GeTe_2 substrate were calculated. Significant renormalization of the electronic bands of Bi(110) induced by the interaction with Fe_3GeTe_2 can be confirmed. As shown in Fig. 4(h), the gray translucent rectangular area highlights the bandgap of Bi(110) without considering Fe_3GeTe_2 substrate. In contrast to the large band gap of pure Bi(110), the band gap of Bi(110) is apparently decreased because of the interlayer interaction with Fe_3GeTe_2 substrate. Also, as indicated by the arrows, significant hole doping effect induced by the Fe_3GeTe_2 substrate is observed. Moreover, the spin-polarized electronic density of states (DOS) of the Bi(110)/ Fe_3GeTe_2 heterostructure is presented in Fig. S4, in which $\text{DOS} > 0$ (< 0) means that spin-up (spin down) states dominate at this energy level. The spin-polarized electronic DOS of non-magnetic Bi(110) should be zero. While, due to the magnetic proximity effect from Fe_3GeTe_2 , a net spin polarization with a magnetic moment of 0.015 μB per Bi atom emerges in the Bi(110)/ Fe_3GeTe_2 heterostructure. The magnetization of Bi(110) very likely originates from the magnetic proximity effect of Fe I atom layer, interfacial charge transfer, and band renormalization. High-precision DOS calculations were also performed for Bi(110)/ Fe_3GeTe_2 heterostructure, and the result [Fig. 4(i)]

shows excellent agreement with the experimental observations, indicating that all above DFT calculation provide a comprehensive simulation of our experimental results.

4 Conclusions

In summary, we have fabricated heterostrain structure composed of 2–3 BL Bi(110) with orthorhombic lattice structure and Fe_3GeTe_2 with hexagonal lattice termination as substrate by MBE. STM characterizations reveal stipes structures of Bi(110) film. Along with strain analysis, bidirectional periodical tensile heterostrain and vibration of buckling height h are found on Bi(110) film. Both periodic biaxial strain and vibration of the buckling height h affect STS results, demonstrating the effective modulation of electronic properties of Bi(110) by the stripe structures, especially for the periodically change of band gap along stripe I. DFT calculated results validate the change of band gap caused by the tensile strain and reveal anisotropic change of Bi p orbitals under strain. We have also investigated the influence of the magnetic substrate Fe_3GeTe_2 on the Bi(110) thin film. The results from the differential charge distribution, band structure modifications, and spin-polarized electronic density calculations demonstrate that magnetic proximity effect exist between BL Bi(110) and Fe_3GeTe_2 substrate. Considering the versatile topological and ferroelectric properties of Bi(110), this interlayer interaction induced periodical strain on a magnetic substrate provides plenty room for further exploration of its novel functionalities. This work demonstrates the potential of straintronics at atomic scale in regulating the electronic structure of 2D vdW heterostructures, offering a pathway to design ultra-thin straintronic and electronic devices.

Declarations The authors declare that they have no competing interests and there are no conflicts.

Electronic supplementary materials The online version contains supplementary material available at <https://doi.org/10.15302/frontphys.2026.045201>.

Acknowledgements This work was supported by the National Natural Science Foundation of China (Grant Nos. 12274016, 12104033, and 12004321), the National Key Research and Development Program of China (Grant Nos. 2022YFB3403400 and 2018YFE0202700), and the Fundamental Research Funds for the Central Universities. The authors acknowledge the facilities and the scientific and technical assistance of the Analysis & Testing Center, Beihang University.

References

1. I. K. Drozdov, A. Alexandradinata, S. Jeon, S. Nadj-Perge, H. Ji, R. J. Cava, B. Andrei Bernevig, and A.



- Yazdani, One-dimensional topological edge states of bismuth bilayers, *Nat. Phys.* 10(9), 664 (2014)
2. T. Nagao, J. T. Sadowski, M. Saito, S. Yaginuma, Y. Fujikawa, T. Kogure, T. Ohno, Y. Hasegawa, S. Hasegawa, and T. Sakurai, Nanofilm allotrope and phase transformation of ultrathin Bi film on Si(111)-7×7, *Phys. Rev. Lett.* 93(10), 105501 (2004)
 3. J. T. Sun, H. Huang, S. L. Wong, H. J. Gao, Y. P. Feng, and A. T. S. Wee, Energy-gap opening in a Bi(110) nanoribbon induced by edge reconstruction, *Phys. Rev. Lett.* 109(24), 246804 (2012)
 4. F. Yang, L. Miao, Z. F. Wang, M. Y. Yao, F. Zhu, Y. R. Song, M. X. Wang, J. P. Xu, A. V. Fedorov, Z. Sun, G. B. Zhang, C. Liu, F. Liu, D. Qian, C. L. Gao, and J. F. Jia, Spatial and energy distribution of topological edge states in single Bi(111) bilayer, *Phys. Rev. Lett.* 109(1), 016801 (2012)
 5. I. Kokubo, Y. Yoshiike, K. Nakatsuji, and H. Hirayama, Ultrathin Bi(110) films on Si(111) 3×3-B substrates, *Phys. Rev. B* 91(7), 075429 (2015)
 6. K. H. L. Zhang, I. M. McLeod, Y. H. Lu, V. R. Dhanak, A. Matilainen, M. Lahti, K. Pussi, R. G. Egdell, X. S. Wang, A. T. S. Wee, and W. Chen, Observation of a surface alloying-to-dealloying transition during growth of Bi on Ag(111), *Phys. Rev. B* 83(23), 235418 (2011)
 7. H. Du, X. Sun, X. Liu, X. Wu, J. Wang, M. Tian, A. Zhao, Y. Luo, J. Yang, B. Wang, and J. G. Hou, Surface Landau levels and spin states in bismuth (111) ultrathin films, *Nat. Commun.* 7(1), 10814 (2016)
 8. J. Gou, L. Kong, X. He, Y. L. Huang, J. Sun, S. Meng, K. Wu, L. Chen, and A. T. S. Wee, The effect of moiré superstructures on topological edge states in twisted bismuthene homojunctions, *Sci. Adv.* 6(23), eaba2773 (2020)
 9. A. Fang, C. Adamo, S. Jia, R. J. Cava, S. C. Wu, C. Felser, and A. Kapitulnik, Bursting at the seams: Rippled monolayer bismuth on NbSe₂, *Sci. Adv.* 4(4), eaaq0330 (2018)
 10. F. Schindler, Z. Wang, M. G. Vergniory, A. M. Cook, A. Murani, S. Sengupta, A. Y. Kasumov, R. Deblock, S. Jeon, I. Drozdov, H. Bouchiat, S. Guéron, A. Yazdani, B. A. Bernevig, and T. Neupert, Higher-order topology in bismuth, *Nat. Phys.* 14(9), 918 (2018)
 11. R. Stühler, A. Kowalewski, F. Reis, D. Jungblut, F. Dominguez, B. Scharf, G. Li, J. Schäfer, E. M. Hankiewicz, and R. Claessen, Effective lifting of the topological protection of quantum spin Hall edge states by edge coupling, *Nat. Commun.* 13(1), 3480 (2022)
 12. L. Peng, J. Qiao, J. J. Xian, Y. Pan, W. Ji, W. Zhang, and Y. S. Fu, Unusual electronic states and superconducting proximity effect of Bi films modulated by a NbSe₂ substrate, *ACS Nano* 13(2), acsnano.8b08051 (2019)
 13. Q. Niu, J. Yao, Q. Song, H. Akber, Q. Zhou, X. Zhai, and A. Zhao, Robust topological interface states in a lateral magnetic-topological heterostructure, *Small* 21(8), 2409979 (2025)
 14. Y. Lyu, S. Daneshmandi, S. Huyan, and C. Chu, Flexible atomic buckling and homogeneous edge states in few-layer Bi(110) films, *Nano Res.* 15(3), 2374 (2022)
 15. Y. Fukushima, K. Kawaguchi, K. Kuroda, M. Ochi, M. Hirayama, R. Mori, H. Tanaka, A. Harasawa, T. Iimori, Z. Zhao, S. Tani, K. Yaji, S. Shin, F. Komori, Y. Kobayashi, and T. Kondo, Spin-polarized saddle points in the topological surface states of elemental bismuth revealed by pump-probe spin- and angle-resolved photoemission spectroscopy, *Phys. Rev. B* 110(4), L041401 (2024)
 16. L. Peng, J. J. Xian, P. Tang, A. Rubio, S. C. Zhang, W. Zhang, and Y. S. Fu, Visualizing topological edge states of single and double bilayer Bi supported on multibilayer Bi(111) films, *Phys. Rev. B* 98(24), 245108 (2018)
 17. H. S. Inbar, M. Zubair, J. T. Dong, A. N. Engel, C. P. Dempsey, Y. H. Chang, S. Nishihaya, S. Khalid, A. V. Fedorov, A. Janotti, et al., Inversion symmetry breaking in epitaxial ultrathin Bi(111) films, arXiv: 2302.00803 (2023)
 18. H. H. Sun, M. X. Wang, F. Zhu, G. Y. Wang, H. Y. Ma, Z. A. Xu, Q. Liao, Y. Lu, C. L. Gao, Y. Y. Li, C. Liu, D. Qian, D. Guan, and J. F. Jia, Coexistence of topological edge state and superconductivity in bismuth ultrathin film, *Nano Lett.* 17(5), 3035 (2017)
 19. S. S. Li, W. X. Ji, J. P. Zhang, Y. P. Wang, C. W. Zhang, and S. S. Yan, Two-dimensional rectangular bismuth bilayer: A novel dual topological insulator, *Front. Phys. (Beijing)* 18(4), 43301 (2023)
 20. J. Gou, H. Bai, X. Zhang, Y. L. Huang, S. Duan, A. Ariando, S. A. Yang, L. Chen, Y. Lu, and A. T. S. Wee, Two-dimensional ferroelectricity in a single-element bismuth monolayer, *Nature* 617(7959), 67 (2023)
 21. Y. Lu, W. Xu, M. Zeng, G. Yao, L. Shen, M. Yang, Z. Luo, F. Pan, K. Wu, T. Das, J. He, J. Jiang, J. Martin, Y. P. Feng, H. Lin, and X. S. Wang, Topological properties determined by atomic buckling in self-assembled ultrathin Bi(110), *Nano Lett.* 15(1), 80 (2015)
 22. W. Luo, Y. Zhong, H. Yu, M. Xie, Y. Chen, H. Xiang, and L. Bellaiche, Topological interfacial states at phase boundaries in two-dimensional ferroelectric bismuth, *Phys. Rev. B* 111(7), 075407 (2025)
 23. Y. Guo, H. Zhu, and Q. Wang, Large second harmonic generation in elemental α -Sb and α -Bi monolayers, *J. Phys. Chem. C* 124(9), 5506 (2020)
 24. C. Xiao, F. Wang, S. A. Yang, Y. Lu, Y. Feng, and S. Zhang, Elemental ferroelectricity and antiferroelectricity in group-V monolayer, *Adv. Funct. Mater.* 28(17), 1707383 (2018)
 25. H. Zhang, B. Deng, W. Wang, and X. Shi, Parity-breaking in single-element phases: Ferroelectric-like elemental polar metals, *J. Phys.: Condens. Matter* 30(41), 415504 (2018)
 26. C. Liu, S. Tao, G. Wang, H. Chen, B. Xia, H. Yang, X. Liu, L. Liu, Y. Li, S. Wang, H. Zheng, C. Liu, D. Guan, Y. Lu, and J. Jia, Tunable topological edge states in black phosphorus-like Bi(110), *Phys. Rev. B* 110(19), 195427 (2024)
 27. K. H. Jin, E. Oh, R. Stania, F. Liu, and H. W. Yeom, Enhanced Berry curvature dipole and persistent spin texture in the Bi(110) monolayer, *Nano Lett.* 21(22), 9468 (2021)
 28. E. Oh, K. H. Jin, and H. W. Yeom, Realizing a super-

- conducting square-lattice bismuth monolayer, *ACS Nano* 17(8), 7604 (2023)
29. S. S. Li, W. X. Ji, P. Li, S. J. Hu, L. Cai, C. W. Zhang, and S. S. Yan, Tunability of the quantum spin Hall effect in Bi(110) films: Effects of electric field and strain engineering, *ACS Appl. Mater. Interfaces* 9(25), 21515 (2017)
 30. Q. Yuan, Y. Li, D. Guo, C. Lou, X. Cui, G. Mei, C. Jiao, K. Huang, X. Hou, W. Ji, L. Cao, and M. Feng, Achieving a large energy gap in Bi(110) atomically thin films, *Small Struct.* 4(12), 2300207 (2023)
 31. Q. Lu, P. V. S. Reddy, H. Jeon, A. R. Mazza, M. Brahlek, W. Wu, S. A. Yang, J. Cook, C. Conner, X. Zhang, A. Chakraborty, Y. T. Yao, H. J. Tien, C. H. Tseng, P. Y. Yang, S. W. Lien, H. Lin, T. C. Chiang, G. Vignale, A. P. Li, T. R. Chang, R. G. Moore, and G. Bian, Realization of a two-dimensional Weyl semimetal and topological Fermi strings, *Nat. Commun.* 15(1), 6001 (2024)
 32. D. J. P. de Sousa, S. Lee, Q. Lu, R. G. Moore, M. Brahlek, J. P. Wang, G. Bian, and T. Low, Ferroelectric semimetals with α -Bi/SnSe van der Waals heterostructures and their topological currents, *Phys. Rev. Lett.* 133(14), 146605 (2024)
 33. C. S. Boland, Y. Sun, and D. G. Papageorgiou, Bandgap engineering of 2D materials toward high-performing straintronics, *Nano Lett.* 24(41), acs.nanolett.4c03321 (2024)
 34. C. Zhang, M. Y. Li, J. Tersoff, Y. Han, Y. Su, L. J. Li, D. A. Muller, and C. K. Shih, Strain distributions and their influence on electronic structures of WSe₂-MoS₂ laterally strained heterojunctions, *Nat. Nanotechnol.* 13(2), 152 (2018)
 35. J. B. Qiao, L. J. Yin, and L. He, Twisted graphene bilayer around the first magic angle engineered by heterostrain, *Phys. Rev. B* 98(23), 235402 (2018)
 36. L. Huder, A. Artaud, T. Le Quang, G. T. De Laissardière, A. G. M. Jansen, G. Lapertot, C. Chapelier, and V. T. Renard, Electronic spectrum of twisted graphene layers under heterostrain, *Phys. Rev. Lett.* 120(15), 156405 (2018)
 37. Y. Huang, M. Manzoor, J. Brndiar, M. Milivojevic, and I. Štich, Straintronics with single-layer MoS₂: A quantum Monte Carlo study, *Phys. Rev. Res.* 6(1), 013007 (2024)
 38. A. A. Bukharaev, A. K. Zvezdin, A. P. Pyatakov, and Y. K. Fetisov, Straintronics: A new trend in micro- and nano-electronics and materials science, *Phys. Uspekhi* 61(12), 1175 (2018)
 39. F. Miao, S. J. Liang, and B. Cheng, Straintronics with van der Waals materials, *npj Quantum Mater.* 6(1), 59 (2021)
 40. W. Xun, X. Liu, Y. D. Zhang, Y. Z. Wu, and P. Li, Stacking-, strain-engineering induced altermagnetism, multipiezo effect, and topological state in two-dimensional materials, *Appl. Phys. Lett.* 126(16), 161903 (2025)
 41. J. Cenker, S. Sivakumar, K. C. Xie, A. Miller, P. Thijssen, Z. Y. Liu, A. Dismukes, J. Fonseca, E. Anderson, X. Y. Zhu, X. Roy, D. Xiao, J. H. Chu, T. Cao, and X. D. Xu, Reversible strain-induced magnetic phase transition in a van der Waals magnet, *Nat. Nanotechnol.* 17(3), 256 (2022)
 42. Y. Wang, H. Sun, C. Wu, W. Zhang, S. D. Guo, Y. She, and P. Li, Multifield tunable valley splitting and anomalous valley Hall effect in two-dimensional antiferromagnetic MnBr, *Phys. Rev. B* 111(8), 085432 (2025)
 43. H. J. Deiseroth, K. Aleksandrov, C. Reiner, L. Kienle, and R. K. Kremer, Fe₃GeTe₂ and Ni₃GeTe₂ - Two new layered transition-metal compounds: Crystal structures, HRTEM investigations, and magnetic and electrical properties, *Eur. J. Inorg. Chem.* 2006(8), 1561 (2006)
 44. Y. Deng, Y. Yu, Y. Song, J. Zhang, N. Z. Wang, Z. Sun, Y. Yi, Y. Z. Wu, S. Wu, J. Zhu, J. Wang, X. H. Chen, and Y. Zhang, Gate-tunable room-temperature ferromagnetism in two-dimensional Fe₃GeTe₂, *Nature* 563(7729), 94 (2018)
 45. I. Horcas, R. Fernández, J. M. Gómez-Rodríguez, J. Colchero, J. Gómez-Herrero, and A. M. Baro, WSXM: A software for scanning probe microscopy and a tool for nanotechnology, *Rev. Sci. Instrum.* 78(1), 013705 (2007)
 46. P. E. Blöchl, Projector augmented-wave method, *Phys. Rev. B* 50(24), 17953 (1994)
 47. G. Kresse and J. Furthmüller, Efficient iterative schemes for ab initio total-energy calculations using a plane-wave basis set, *Phys. Rev. B* 54(16), 11169 (1996)
 48. J. P. Perdew, K. Burke, and M. Ernzerhof, Generalized gradient approximation made simple, *Phys. Rev. Lett.* 77(18), 3865 (1996)
 49. S. Grimme, J. Antony, S. Ehrlich, and H. Krieg, A consistent and accurate ab initio parametrization of density functional dispersion correction (DFT-D) for the 94 elements H-Pu, *J. Chem. Phys.* 132(15), 154104 (2010)
 50. M. J. Hÿtch, E. Snoeck, and R. Kilaas, Quantitative measurement of displacement and strain fields from HREM micrographs, *Ultramicroscopy* 74(3), 131 (1998)